

Cite this: DOI: 00.0000/xxxxxxxxxx

Pursuing colloidal diamond[†]Łukasz Baran,^{*a} Dariusz Tarasewicz,^a Daniel M. Kamiński^{b‡}, and Wojciech Rzyśko^aReceived Date
Accepted Date

DOI: 00.0000/xxxxxxxxxx

The endeavor to selectively fabricate cubic diamond is challenging due to the formation of competing phases such as its hexagonal polymorph or others possessing similar free energy. The necessity to achieve that is of paramount importance, since the cubic diamond is the only polymorph exhibiting a complete photonic bandgap making it a promising candidate in view of photonic applications. Herein, we demonstrate that due to the presence of external field and delicate manipulation of its strength we can attain the selectivity in the formation of cubic diamond in a one-component system comprised of designer tetrahedral patchy particles. The driving force of such phenomena is the structure of the first adlayer which is commensurate with (110) face of the cubic diamond. Moreover, after a successful nucleation event, once the external field is turned off, the structure remains stable, paving an avenue for a further post-synthetic treatment.

1 Introduction

Crystallization of hard spheres has been a matter of a long-standing scientific discussion. It has been found that the experimental realization of such systems can be done by the application of dispersed colloidal particles of, for instance, polymethylmethacrylate dissolved in a non-polar solvent.^{1,2} This result was particularly useful, as colloidal crystals have a size comparable to visible light, therefore making them particularly appealing in the context of photonic crystal synthesis. Photonic crystals or photonic band gap structures are three-dimensional periodic dielectric materials that are to photon waves as semiconductor crystals to electron waves making them potentially useful for controlling the propagation of light.³ Such structures are omnipresent in nature, ranging from gem and opals formed by precipitative settling processes to wing scales or barbules of some insects and bird feathers.⁴ In view of the photonic applications, open lattices such as diamond⁵ or tetrastack^{6,7} serve to be great candidates since in both cases the cubic polymorph exhibits a complete photonic band gap. Isotropic particles, however, possess the tendency to form the structures of the highest packing fraction in which the stability is controlled by the nearest neighbors with a similar local environment, resulting in the formation of two competing networks i.e. face-centered cubic (fcc) and hexagonal close-packing (hcp) crystals.

The endeavor to selectively fabricate colloidal cubic diamond is a formidable task. In recent years, a few routes have been utilized for the design of such tetrahedral open lattices. In this respect, patchy particles have been extensively used^{7–16}. The most straightforward approach is to distribute the patches over the spherical core of the particle matching the symmetry of the desired crystal structure. Although this seems to be a quite feasible way, tetrahedral patchy particles exhibit a quite complex phase diagram which includes crystallization into stacking hybrids of interlaced hexagonal (DH) and cubic diamonds (DC)^{8,9,12}. Enforcement of the directionality of interparticle interactions does not seem to alleviate these issues as the formation of empty clathrate cages is now preferred¹⁵. All these obstacles result in that precise control over the nucleation process becomes extremely challenging. It is therefore of paramount importance to find directions for the selectivity in the synthesis of the target crystalline structure and to circumvent the undesired coexistence with the second phase.

Several routes have been utilized to alleviate the aforementioned issues. To list a few, the assembly of tetrahedral DNA origami constructs acting as host molecules caging guest gold nanoparticles coated with single-stranded DNA was utilized to form a cubic diamond superlattice¹⁷. Similarly, cooperative self-assembly of tetrahedra and isotropic spherical particles lead to the formation of diamond and pyrochlore crystals¹⁸. Recently, it has been demonstrated that the use of tetrahedral clusters with partially embedded patches lead to the selective formation of the cubic diamond crystal in a single-component systems¹⁹. The idea lies behind the excluded volume effects which forbid the aggregation of the building blocks into the eclipsed conformation, necessary for the the emergence of the hexagonal diamond.

Patchy particles have also been extensively studied by the

^a Department of Theoretical Chemistry, Institute of Chemical Sciences, Faculty of Chemistry, Maria-Curie-Skłodowska University in Lublin, Pl. M Curie-Skłodowskiej 3, 20-031 Lublin, Poland E-mail: lukasz.baran@mail.umcs.pl

^b Department of Organic and Crystallochemistry, Institute of Chemical Sciences, Faculty of Chemistry, Maria-Curie-Skłodowska University in Lublin, Pl. M Curie-Skłodowskiej 3, 20-031 Lublin, Poland

[†] Electronic Supplementary Information (ESI) available: See DOI: 00.0000/00000000.

means of computer simulations. For instance, Romano and Sciortino¹² demonstrated that triblock patchy particles with spherical patches crystallize simultaneously into two tetrastack polymorphs. However, patterning the patches into triangular shape results in the selective formation of a cubic tetrastack structure or clathrates, depending on the relative orientation of the patches. The idea of patterning the patches is based on the seminal paper by Zhang et al.¹⁶ where they introduced additional potential energy term between pairs of bonded particles that induced relative orientations favoring staggered conformation. Similar studies have been performed for triblock patchy particles with patches different in nature^{7,13,20}. Utilization of the so-called “self-limiting” approach in which patchy particles form tetrahedral clusters which cease to grow further under certain conditions and instead act as a secondary building block. Such a two-stage self-assembly route hinders the formation of different undesired structures, partly due to the monodispersity attained in the first step of the assembly process. Sun *et al.*¹⁰ also proposed an alternative route for the nucleation of colloidal photonic crystals which involved the utilization of cooperative self-assembly of triblock patchy particles with spherical colloids, similar to the experimental realization¹⁸. Binary mixtures of tetrahedral patchy particles have also been studied quite recently^{21,22}. It is also worth emphasizing that these studies, although performed *in silico*, seem not to be challenging to be performed experimentally in view of the recent advances in the patchy particle synthesis^{19,23–27}.

In spite of the recent successes, a comprehensive understanding of the conditions for the selective formation of colloidal diamonds is yet to be achieved. Here we demonstrate another alternative route to attaining the cubic diamond polymorph by precise control over the system parameters by employing the bottom-up self-assembly strategy for tetrahedral patchy particles in one-component system. Due to the presence of the external field and delicate manipulation of its strength the diamond networks start to nucleate differently and the driving force of the process is the structure of the first adlayer. The change in its structure leads to a change in the nucleation mechanism and to the selective emergence of the cubic diamond lattice. Moreover, once the external field is turned off, the structure remains stable which gives an opportunity for a further post-synthetic treatment.

2 Methods

Model details

In this work, we employ a similar approach as already used in our previous papers^{28,29}. The patchy particle model is comprised of the spherical core of the diameter σ_p on which surface four attractive patches of size σ_a are spatially distributed in tetrahedral arrangement and are embedded to a certain extent. The parameter l describing the latter depicts the joining distance between the centers of a core and each of the four patches (cf. Fig. 1). We have shown that such an approach can be successfully used to mimic directional interactions. Moreover, by the precise control over the patch size and its embedment distance l , one can attain a specific and desired patch’s valency which we have proven to be nearly equivalent to the one used within the standard routine of

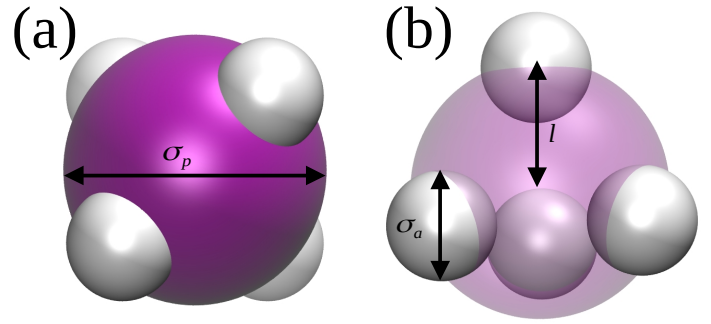


Fig. 1 Schematic representation of the parameters of the model for tetrahedral patchy particles. Central spherical core and active sites are schematically represented (scale is not preserved) by purple and white spheres, respectively.

Kern-Frenkel potential^{28–30}. The patchy particles interacted via truncated and shifted Lennard-Jones (12,6) potential in which there is no discontinuity in the forces. In the following, $\sigma_p = \sigma$ and ϵ_{pp} have been defined to be the units of distance and energy, respectively. In the current simulations, we have chosen the set of parameters to be equal $\sigma_a = 0.2\sigma$ and $l = 0.36\sigma$ and have been devised to allow for the association of only pairs of patches resulting in that every patchy particle could create four bonds in total. Moreover, we fixed the association energy to be $\epsilon_{aa} = 5.0\epsilon$ whereas $\epsilon_{pp} = 1.0\epsilon$. The range of interparticle interactions was set to be $r_{cut,aa} = 2.0\sigma_{aa}$ and $r_{cut,ij} = \sigma_{ij}$ otherwise ($ij = pp, pa$). This indicates that the only attraction in the system was due to the association between different patches and the remaining interactions were soft-repulsive. Embedding an active site to the certain extent which is controlled by the parameter l results in that the spherical Lennard-Jones potential is screened for certain orientations of patchy particles. In effect, causing that one can control the directionality of the interparticle interactions. Larger values of l than $l = 0.36\sigma$ lead to that one association site can create multiple bonds which was an undesired effect within the scope of current study (Supporting Information).

In order to maintain the rigidity and the desired geometry of our tetrahedral particles, we used harmonic spring potentials for bonds and bond angles. The harmonic spring constants were set to be $k_b = 1000\epsilon/\sigma^2$ and $k_\theta = 1000\epsilon/rad^2$ to ensure that the fluctuations in all the necessary bond and bond angles are negligible.

On top of the interparticle interactions, we introduced the effects of the spatial constraints by the means of the flat, structureless wall modeled by the Lennard-Jones (9,3) potential is defined as follows:

$$U^{ext}(z) = \epsilon_{wc} \left[\frac{2}{15} \left(\frac{\sigma}{z} \right)^9 - \left(\frac{\sigma}{z} \right)^3 \right] \quad \text{if } z \leq 5\sigma \quad (1)$$

where ϵ_{wc} indicates the depth of potential well for interactions.

The potential acted solely on the core of the patchy particle which on the one hand should not interrupt the self-assembly behavior but on the other hand, it can be thought of as the introduction of isotropy on how the patchy particles will be arranged

with respect to the wall. Moreover, since the employed potential is uniform, it can be viewed as the presence of any external field and the change in the ratio ξ of attraction strengths defined as $\xi = \frac{\epsilon_{wc}}{\epsilon_{aa}}$ should be universal within the range of the same exact phenomena.

Simulation protocol

All of the molecular dynamics simulations have been launched by the use of LAMMPS simulation package³¹. Trajectories were evolved using the velocity Verlet algorithm, with a timestep of $\tau = 0.001$. The temperature has been maintained by the use of Nosé-Hoover chains thermostat with damping factor $\tau_{NH} = 10\tau$. The systems comprised of 2500 or 16129 for systems under confinement to check for possible finite-size effects and the surface density was fixed to allow for the formation of seven close-packed monolayers. Therefore, the system size $L_x \times L_y \times L_z$ was equal to $18 \times 18 \times 40$ ($48 \times 48 \times 40$) in x, y, z directions for 2500 (16129) patchy particles, respectively. Bulk systems were composed of 3375 or 15625 patchy particles at distinct densities ranging from $\rho = 0.2$ to $\rho = 1.2$. Each of the systems was gradually cooled down from disordered states with an increment in temperature equal to $\Delta T = 0.01$. Once the parameter $c_3(i, j)$ indicated the nucleation event, the increment was changed to $\Delta T = 0.005$. Simulations were launched for $2 \times 10^8 - 4 \times 10^8$ simulation steps at every thermodynamic state for the equilibration period. Further production runs were launched for at least 10^7 timesteps. Five independent replicas have been launched in order to present reliable results and to calculate the error which are presented in terms of standard errors.

Block analysis

The bulk phase diagram has been determined by using finite size scaling of the block density distribution functions following the method proposed by Binder³². The simulation cell at distinct densities ranging from $\rho = 0.2$ to $\rho = 1.2$, has been divided into blocks of different sizes. Then, the density probability distributions for patchy particles $P(\rho)$ normalized so that the integral equals unity, have been estimated for each block. An example of such a distribution function exhibiting double-peak behavior, corresponding to the two-phase coexistence is shown in Supporting Information. The densities of coexisting phases have been taken from the maxima of these distribution functions at every considered temperature.

Crystal identification

In order to quantify the formed three-dimensional crystalline networks, we employed a standard routine involving the calculation of Steinhardt order parameter³³ given by:

$$q_l = \sqrt{\frac{4\pi}{2l+1} \sum_{m=-l}^{m=l} |q_{lm}|^2} \quad (2)$$

with

$$q_{lm} = \frac{1}{N_b(i)} \sum_{j \in N_b(i)} Y_{lm}(\theta_{ij}, \phi_{ij}) \quad (3)$$

where Y_{lm} are spherical harmonics and for a given sphere i , we choose a set of its nearest neighbors, $N_b(i)$. We define that any two spherical particles connected by a bond if they are neighbors,

that is, if $j \in N_b(i)$. For a particle i , the set of unit vectors \mathbf{n}_{ij} points from i to the particle $j \in N_b(i)$ in the neighborhood of i . Each vector \mathbf{n}_{ij} is characterized by its angles in spherical coordinates θ_{ij} and ϕ_{ij} on the unit sphere, evaluated between the bond and an arbitrary but fixed reference frame. The set of all bond vectors is called the bond network.

Discrimination between diamond networks is based on the correlation function $c_l(i, j)$ ³⁴ defined as:

$$c_l(i, j) = \frac{\sum_{m=-l}^{m=l} q_{lm}(i) q_{lm}^*(j)}{\left(\sum_{m=-l}^{m=l} q_{lm}(i) q_{lm}^*(i) \right)^{1/2} \left(\sum_{m=-l}^{m=l} q_{lm}(j) q_{lm}^*(j) \right)^{1/2}} \quad (4)$$

Particles in a crystalline environment were labeled using $c_3(i, j)$. Two particles are connected by a staggered bond when $c_3(i, j) \leq -0.8$ and an eclipsed bond when $-0.05 \geq c_3(i, j) \geq -0.2$. Afterward, molecules with exactly four neighbors were further discriminated as cubic diamond if they were connected with one another by four staggered bonds or hexagonal diamond which has three staggered bonds and one eclipsed bond.

Characterization of the primary adlayer

Another quantity that allows one to identify two-dimensional ordering, including discrimination between the hexagonal and Kagomé structures (and other) has been proposed quite recently^{35,36}. It is defined as follows:

$$\lambda_1(i) = \frac{1}{N_b(i)} \sum_{j \in N_b(i)} \left[\sum_{m=-6}^6 \hat{q}_{6m} \hat{q}_{6m}^* - \sum_{m=-4}^4 \hat{q}_{4m} \hat{q}_{4m}^* \right] \quad (5)$$

and

$$\lambda_2(i) = \frac{1}{N_b(i)} \sum_{j \in N_b(i)} \left[\sum_{m=\pm 6, \pm 4} \hat{q}_{6m} \hat{q}_{6m}^* - \sum_{m=\pm 4} \hat{q}_{4m} \hat{q}_{4m}^* \right] \quad (6)$$

where

$$\hat{q}_{lm} = \frac{q_{lm}(i)}{\left(\sum_{m=-l}^l |q_{lm}(i)|^2 \right)^{1/2}} \quad (7)$$

The hexagonal network is identified in the order parameter space (λ_1, λ_2) with the values of $(0.0, 0.8)$. Note that these values correspond to the perfect lattices and to account for that, we allowed for 10% uncertainty during the discrimination procedure. The degree of the order has been further evaluated as the ratio of the number of patchy particles in the hexagonal environment N_{hex} and the total number of particles belonging to the first adlayer N_{lay} , i.e.

$$P_{\text{hex}} = \frac{N_{\text{hex}}}{N_{\text{lay}}} \quad (8)$$

Calculated observables

Aside from the aforementioned parameters, the calculation of density profiles $\rho(z)$, in the direction perpendicular to the wall

has been performed. This parameter supports the analysis and allows one to discriminate the crystallographic direction of the growth of the formed solid network and provides a hint at the spatial arrangement of the three-dimensional structure.

Another quantity, describing the surface behavior considered systems of interest, was the excess adsorption Γ which is defined as follows

$$\Gamma = \int_0^{\infty} (\rho(z) - \rho_b) dz \quad (9)$$

with ρ_b being the bulk density. In order to avoid the effect of the presence of the second reflective wall, the upper limit in the integral was taken as $L_z - 4$.

To characterize the ‘‘roughness’’ of the adsorbed crystalline film, we calculated the distribution of the film height. The simulation cell in the xy-plane has been divided in the blocks of $1.0\sigma \times 1.0\sigma$ size. In each of such bins, the maximum position value in the z-direction of an atom belonging to the crystalline network has been recursively evaluated. Then, the film height probability distribution $P(h)$ is normalized so that the integral is equal to unity.

3 Results

Bulk phase diagram

In order to accurately demonstrate the effect of the applied external field, we begin the discussion with the evaluation of the bulk phase diagram for our designer tetrahedral patchy particles (cf. Fig. 2 (a)). The patchy particles were devised such that the interactions resulted in a single association. The evaluation of the bulk phase diagram was done by means of the block analysis proposed by Binder³². An example of the distribution function exhibiting double-peak behavior corresponding to the two-phase coexistence can be found in Supporting Information.

It is evident that the phase diagram, shown in Figure 2 (a) is similar to the one reported by Romano *et al.*⁹ for the Kern-Frenkel model. In such a diagram, there is a gas-solid coexistence with a narrow (or not at all) metastable liquid region. A detailed description of how we envisaged the latter can be found in Supporting Information. This is particularly beneficial because the super-cooled liquid phase usually has similar free energy to the crystal phases resulting in strong competition between the formation of kinetically arrested glasses and diamond crystals. We conjecture that the inhibition of the emergence of a liquid phase, which is mainly due to the insufficient range of interparticle interactions, makes the crystallization process much more feasible. The latter conclusion apart from the works by Romano *et al.*^{8,9}, can be supported by the study of Trokhymchuk *et al.*³⁷ which although performed in 2D, suggests such behavior should be universal.

However, similar to the previous studies, encountering the formation of stacking hybrids of cubic and hexagonal diamonds is inevitable. The discrimination between different local crystalline environments has been performed based on the $c_3(i, j)$ parameter. Since these structures belong to different space groups being $Fd\bar{3}m$ and $P6_3/mmc$ for cubic and hexagonal polymorphs, respectively, such assembling can only be possible along the (111) di-

rection of the former and (0001) of the latter (cf. Fig 3). Such a combination, although being described by a hexagonal unit cell, does not belong to any of the two space groups and has a trigonal $P3m1$ space group, instead³⁸.

The value of order parameter is equal to $c_3(i, j) = -1$ and $c_3(i, j) = -0.1$ for staggered and eclipsed bonds, respectively. Figure 2 (b) demonstrates the distribution function $P(c_3)$ for two replicas differing in the ratio of cubic and hexagonal diamonds. As these structures differ by just one eclipsed bond, the height of the distribution function around $c_3(i, j) = -0.1$ is different depending on the crystal composition. The representative snapshots corresponding to the distribution functions are shown in parts (c, d) of Figure 2. It is worth noticing that the crystallization process in bulk systems changes from replica to replica and does not necessarily lead to the formation of one single crystalline network (cf. Fig 2 (c)) but can result in growth in several competing directions (cf. Fig 2 (d)). As will be shown later, the introduction of the directionality of the nucleation process may result in the prohibition of the formation of stacking hybrids. However, it is noteworthy that such interlaced stacking arrangements of cubic and hexagonal diamonds have also been found in other tetrahedral systems, such as water, diamond, or silver iodide to list a few^{38–41}.

External field-driven self-assembly

Relying on the evaluated bulk phase diagram, we can comprehensively assess the effect of the applied external field. The discussion will be based on the introduction of the parameter ξ depicting the ratio of the strengths of particle-wall and particle-particle energies. We identified three different regimes on how the designer patchy particles nucleate depending on the value of ξ . These findings are mainly supported by the density profiles $\rho(z)$ (cf. Fig. 4 (a)), the order parameter $c_3(i, j)$ required for the discrimination between the diamond phases, and the excess adsorption curves (cf. Fig 4 (c)).

In the first case, $\xi = 0.4$, indicating that the patch-patch interactions prevail, we observe the emergence of similar stacking hybrids as in the bulk phase (Supporting Information). A characteristic bilayer structure perpendicular to the z-axis can be seen, indicating the (0001) or (111) faces of hexagonal and cubic diamonds, respectively. The composition of the formed crystalline network has been described by the cubicity parameter defined as $N_{CD}/(N_{CD} + N_{HD})$ with N_{CD} and N_{HD} being the numbers of patchy particles belonging to cubic or hexagonal diamond networks, respectively, plotted in Fig. 4 (b). Moreover, for such a small value of confining energy, we barely see any adsorption and the density profile resembles a bulk-like one. Large error bars in the cubicity curve over an entire temperature range also prove the behavior to be similar to the bulk where the composition of the formed crystalline networks is replica-dependent.

Increasing the strength of the external field to $\xi = 0.6$ only slightly changes the behavior of the system. From the density profile, the emergence of the first layer differing significantly from the other part of the system is evident (cf. Fig 4 (a)). However, in spite of that, the first adlayer is not ordered, which has been

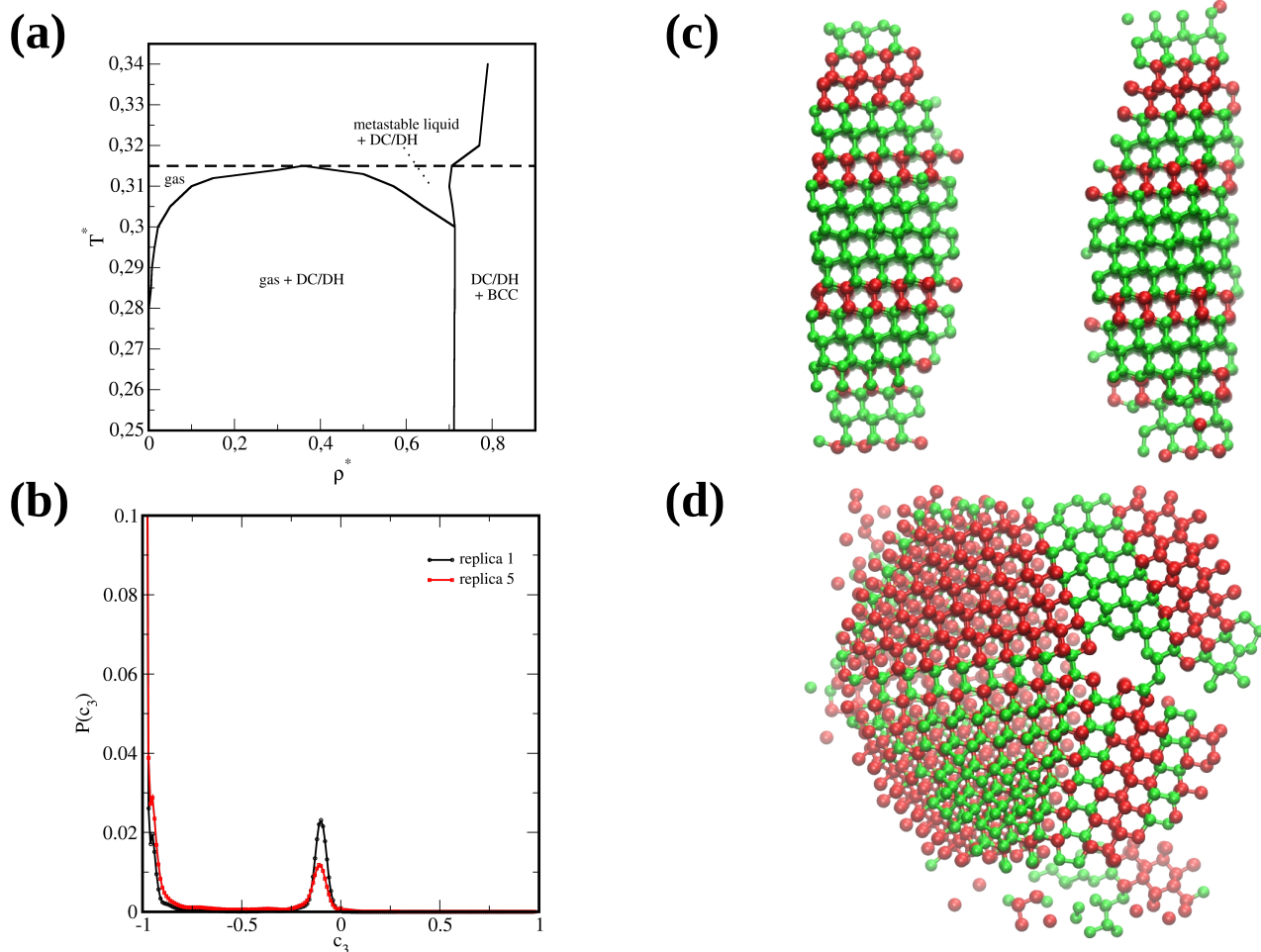


Fig. 2 Part (a): Bulk phase diagram. Part (b): Distribution functions of the order parameter $P(c_3)$ for two distinct replicas differing in the crystal composition. Parts (c), (d): Snapshots corresponding to the distribution functions shown in part (b). Red and green sticks and atoms correspond to the cubic and hexagonal diamond environments, respectively.

assessed by means of (λ_1, λ_2) 2D order parameters introduced by Müller-Plathe's group. It is also noteworthy that shifting the density profiles by $1/3\sigma$ in the z-axis, leads to the overlap with the $\xi = 0.4$ case, indicating similar behavior (see Supporting Information). This is also demonstrated by the cubicity parameter whose value fluctuates around 0.6 with quite large deviations. The overall structure resembles the one obtained in bulk or for $\xi = 0.4$ which can be seen in Fig. 4 (d).

A further increase of the confining energy to $\xi = 0.8$ completely changes the behavior of the system. For the current case, we see that the characteristic bilayer structure perpendicular to the z-axis is no longer present, indicating that the crystal growth mechanism changes. Moreover, the cubicity parameter increases up to 0.8. The snapshot displayed in Fig. 4 (e) demonstrates that the formed crystalline network is completely different than in the previous cases. The emergence of (110) face which is a characteristic plane for a cubic diamond can be observed. The imperfections are also present, however, their origin is due to the tilt in the crystal nucleus. In such cases, if the growth is tilted by 45° the (111) face becomes exposed and in consequence, the stack-

ing hybrid may form. The overall features presented for $\xi = 0.8$ are even more pronounced for systems with $\xi \geq 1$. Complementary snapshots for different replicas in these systems are shown in Supplementary Information.

Since we are examining systems differing in the strength of the confining energy, it is instructive to check how the adsorbed film grows on the surface. In order to do that, we calculated the excess adsorption and its temperature variation is shown in Fig. 4 (c). In general, it has been established that there are three main scenarios on how the film can grow on solid substrates^{43,44}. In the first one, when the surface adhesion dominates the cohesive interactions, the film grows asymptotically toward the infinite thickness (Frank-van der Merwe: type-1). In the second mechanism, when the surface interactions are weaker, the film reaches a finite thickness usually only a few molecular layers thick (Stranski-Krastanov: type-2). Eventually, when the interparticle interactions prevail, the adsorption is small under any conditions (Volmer-Weber: type-3).

In currently investigated systems, we can see that the system with $\xi = 0.4$ displays a type-3 behavior whereas $\xi = 0.6$ and

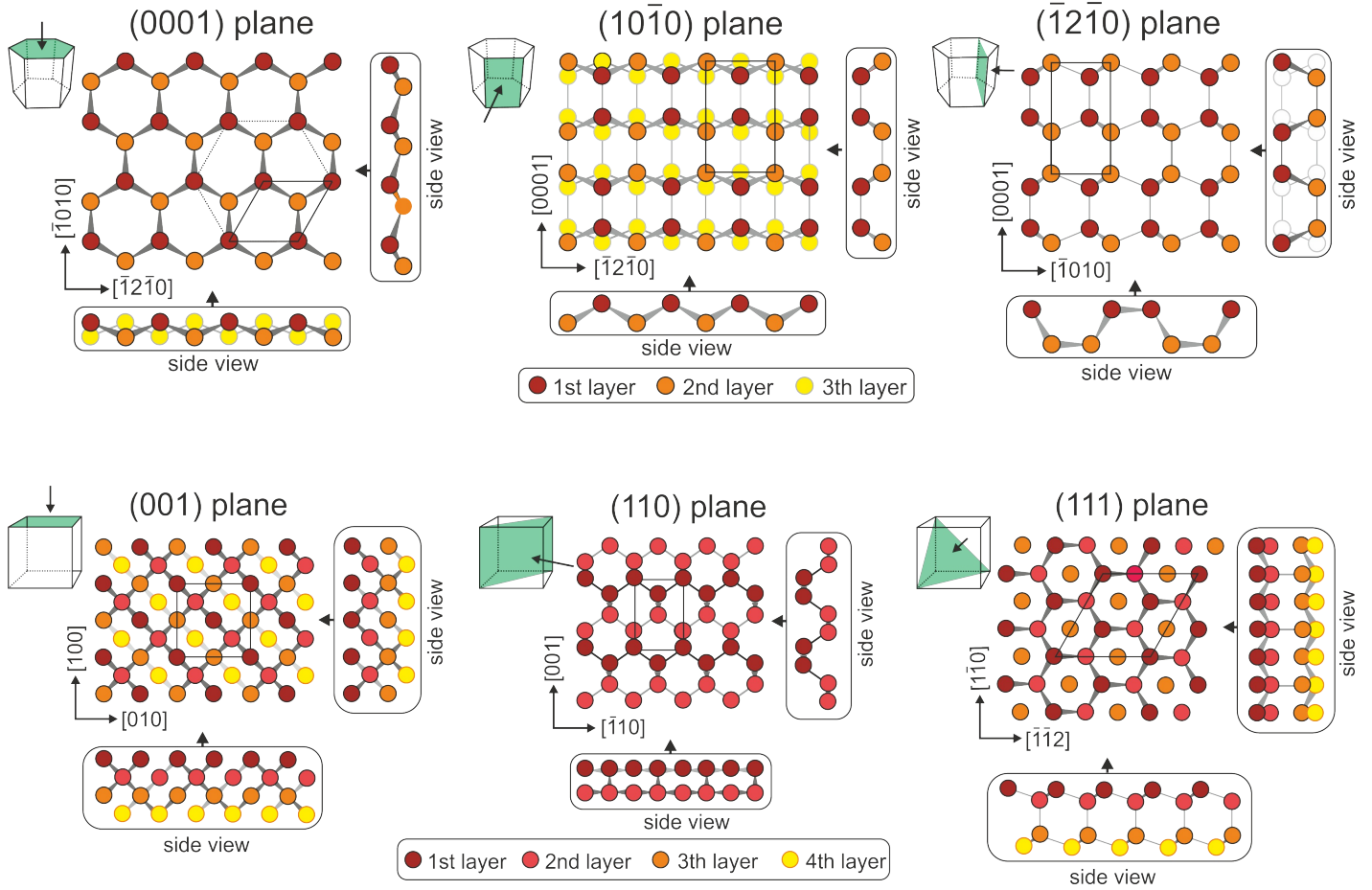


Fig. 3 Schematic representation of symmetry faces of hexagonal (top panel) and cubic diamond lattices (bottom panel). The sketch is based on the one reported in ref⁴².

$\xi = 0.8$ present type-2 behavior. All such observations can be confirmed by the inspection of the density profiles (Fig. 4 (a)). A characteristic jump in the value of Γ is observed for all such cases and further continuous growth is observed with a decrease in temperature. With further increase in the confining energy, we can see that for $\xi \geq 1$ the growth mechanism changes to be type-1. In such instances, usually one should observe the epitaxial layer-by-layer growth appearing as a series of layering transitions, however, we find a continuous increase of excess adsorption, instead. We conjecture that the origin of such discrepancy is twofold. The simulation time and the cooling step can be insufficient for these transitions to reveal. Moreover, as already mentioned, for some replicas we observe that the crystal can be slightly tilted which leads to the irregular structure of the surface. As we are characterizing the *average* value of excess adsorption and not the *distribution* in the xy -plane we are neglecting the surface fluctuations which may also explain the absence of layering transitions. The aspect of the nature of surface phase transitions should therefore be further studied.

Being acquainted with the behavior of the currently examined systems, a naturally arising question can be cast: what is the driv-

ing force of such a reorientation resulting in the selective formation of the cubic diamond? Why does the increase in the strength of the external field causes such a difference in the nucleation mechanism? Here, we aim to answer that with the support of (λ_1, λ_2) order parameter. This parameter is particularly useful in terms of the characterization of two-dimensional networks as in the current case of the first adsorption layer. We already mentioned the fact that for $\xi = 0.6$, despite that there is a significant adsorption layer formed, it is not ordered. The first system in which the set of parameters (λ_1, λ_2) identify the formation of the hexagonal network (up to $P_{\text{hex}} = 0.2$) is $\xi = 0.8$. Simultaneously, on the density profiles $\rho(z)$ we see that the crystal growth mechanism changes. Such behavior is even more explicit for $\xi \geq 1.0$ where P_{hex} reaches values close to 0.9 indicating significant ordering in the first adlayer.

In order to demonstrate the mechanism governing the emergence of (110) face of cubic diamond, we refer to Figure 5. In panel (a), the primary adsorption layer of hexagonal structure is shown together with its hexagonal (blue lines) and rectangular unit cells (yellow lines). Part (b) of Figure 5 displays the consecutive layer which is (110) face of cubic diamond which has

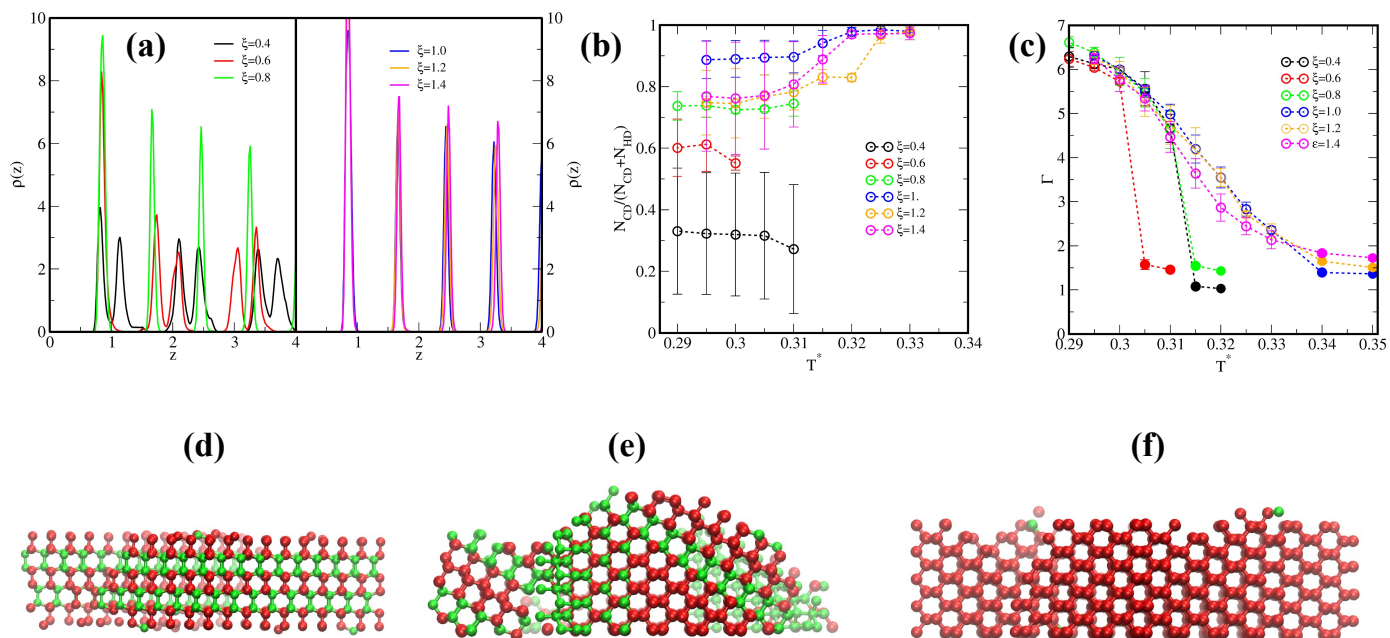


Fig. 4 Part (a): Density profiles for considered systems under different strengths of an applied external field. Parts (b), (c): temperature relation of the cubicity parameter and excess adsorption for all considered systems. Parts (d)-(f): Snapshots demonstrating different crystal growth mechanisms depending on the strength of the surface potential; $\xi = 0.6$ (d), $\xi = 0.8$ (e), $\xi = 1.0$ (f). Red and green sticks and atoms correspond to the cubic and hexagonal diamond environments, respectively.

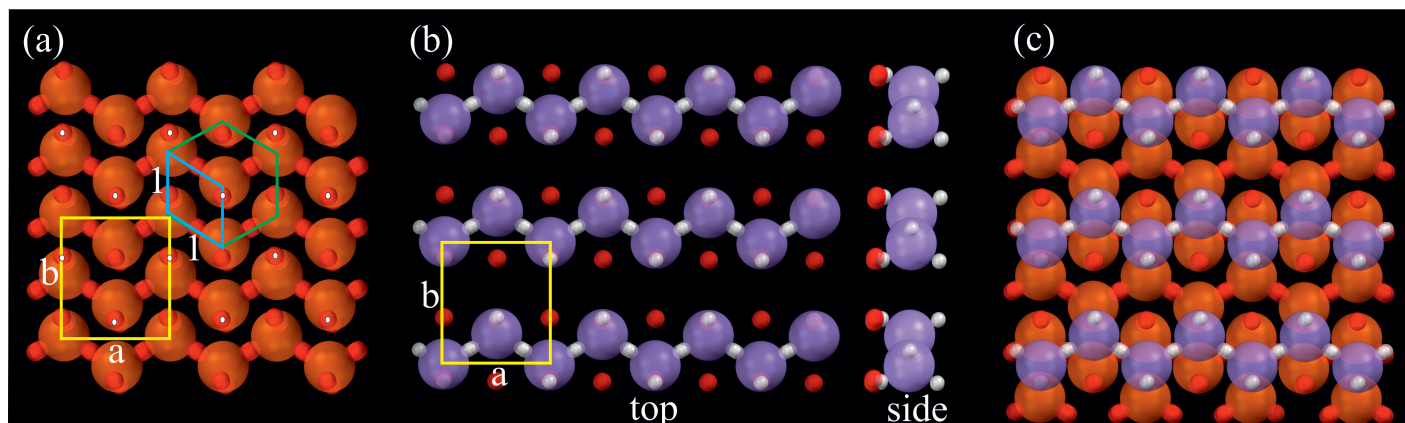


Fig. 5 Part (a): Snapshot of the primary adlayer of hexagonal structure with the hexagonal (blue lines) and rectangular unit cells (yellow lines). $a = 1.73\sigma$ and $b = 2.0\sigma$. Active sites forming bonds with the upper layer are marked with white dots. Part (b): Top and side view on the consecutive layer displaying the (110) face of cubic diamond which has the same vectors in its rectangular unit cell as the hexagonal adlayer from part (a). Part (c): Snapshot showing how these two layers from parts (a), (b) are spatially arranged one with another. Orange and purple atoms are used to pronounce the ordering and spatial arrangement.

identical rectangular unit cell as the hexagonal layer shown in panel (a). Figure 5 (c) shows how these two layers are spatially arranged one with another. This now seems to be clear that the commensurability of the (110) face of cubic diamond and the hexagonal lattice has the most significant impact on the selective formation of the cubic diamond network.

Removing external field

In the previous section, we demonstrated that increasing the external field results in the selective emergence of the cubic diamond network that is compatible with the structure of the first adlayer. Therefore, a naturally arising question is, what happens when the external field is turned off? Figure 6 demonstrates the absolute ratio of the number of molecules belonging to either of the diamond phases (N_{CD} or N_{HD}) to the total number of patchy particles in the system for several values of the parameter ξ . For $\xi = 1$ (Fig. 6 (a)), we see that once over 60% of the system crystallized into cubic diamond, the removal of the external field causes further growth of the formed phase. The same concerns $\xi = 0.6$ and $\xi > 1$ cases (Supporting Information). For $\xi = 0.4$ the situation is slightly different as the removal of an external field does not change anything since the system behaves as a bulk-like (type-3 growth mechanism) irrespectively (Supporting Information).

However, the above refers to the low-temperature configurations with quite a large nuclei in the range of the bulk phase diagram, where such crystal networks are stable. Therefore, for $\xi = 1$ we checked what would happen once the nucleus is comprised of several hundred atoms. Since the phase diagram terminates above $T^* = 0.315$ with a (metastable) critical point, we took the configurations from higher temperatures, i.e. $T^* = 0.33$ and $T^* = 0.325$ and cooled it down to $T^* = 0.31$, so within the bulk stability region, and results are shown in Figure 6 (b). In the former, the initial nucleus of a cubic diamond comprised of merely 150 tetrahedral patchy particles grows further, however after enough time, the formation of a competitive hexagonal diamond can be seen. In the second case, the initial nucleus was larger and composed of around 400 patchy particles and the defects are not present within the considered simulation time.

These findings are crucial for the following reasons. The most important is that the application of the confining potential can be used to tune the architecture of the self-assembled networks in the system comprised of tetrahedral patchy particles which remain stable even if the external field is turned off. Moreover, we demonstrated that the external field can be used as an initial tool to increase the density next to the surface and to create an initial nucleus that, if large enough, continues to grow into the same network. Both of these aspects open up an avenue for the post-synthetic treatment of these colloidal diamond crystals that can be potentially useful for photonic applications.

System size effects

As the nucleation process is an activated event, we see that despite being able to selectively obtain the cubic diamond for most of the replicas, in some cases, the growing crystal is tilted by 45°

relative to the surface, exposing the (111) face of a cubic diamond and giving rise to the formation of stacking hybrids. We envisage, that since our studies are performed in NVT ensemble, the lateral directions are not able to fluctuate and adjust according to the lattice parameters of the forming crystals. In consequence, frustrations emerge, and the resulting imperfections may affect the growth process.

To verify our hypothesis, we performed auxiliary simulations for system sizes comprising of 16129 designer patchy particles, corresponding to approximately seven times larger surface area.

The results are qualitatively identical to those presented for a smaller system consisting of 2500 particles and can be found in Fig. 7. The density profiles displayed in part (a) are identical to those for a smaller system. However, as expected, the frustrations that were present in the smaller system vanish which is demonstrated by the values in the cubicity parameter (cf. Fig. 7 (b) and Fig. 4 (b)) for systems with $\xi \geq 1.0$. It is evident that these systems are comprised of a cubic diamond crystal over an entire temperature range. Within all five replicas, we did not spot any significant defects arising from the emergence of competing hexagonal diamond.

Another aspect worth highlighting regards the type-1 growth mechanism (cf. Fig 4 (c)) whose emergence was not revealed due to surface fluctuations which are neglected in the calculation of the average excess adsorption. Snapshots of large systems for $\xi = 1.0$ and $\xi = 1.2$ seem to corroborate that assumption where one can clearly see a large differences in the film height in the xy -plane. To demonstrate that, we calculated the distribution of the film height $P(h)$ which is shown in Figure 8. Part (a) display the comparison of the distribution $P(h)$ for different strengths of the surface potential. We can see that these systems, although having the value of excess adsorption of $\Gamma \approx 6$ (cf. Fig. 4 (c)), are significantly different from one another. System for $\xi = 0.6$ exhibit the largest film height, as expected due to the type-1 growth mechanism. With the increase of the strength of confining potential, film height decreases, indicating that the layers tend to grow more uniformly, in a layer-by-layer fashion (type-2 or type-3 mechanisms). Part (b) on the other hand, shows results for the system $\xi = 1.0$ and demonstrate that even for such large system sizes, we still observe the differences between distinct replicas.

Moreover, this is particularly interesting since the formed cubic crystals expose their (111) face and unlike in the small system, the hexagonal polymorph does not grow. This observation supports our previous suspicion that the emergence of a competitive crystalline network originates from frustration due to insufficient surface size which on top of that cannot fluctuate in NVT simulations. Now it seems to be clear that large enough system sizes alleviate the issues encountered by insufficiently large systems. This finding is crucial and demonstrates the importance of finite-size effects in computer simulations and the need for using multiple replicas in order to attain representative results.

4 Conclusions

In this paper, we performed a molecular dynamics simulation study demonstrating the possibility of the selective formation of the cubic diamond lattice. The process relies on the use of an ex-

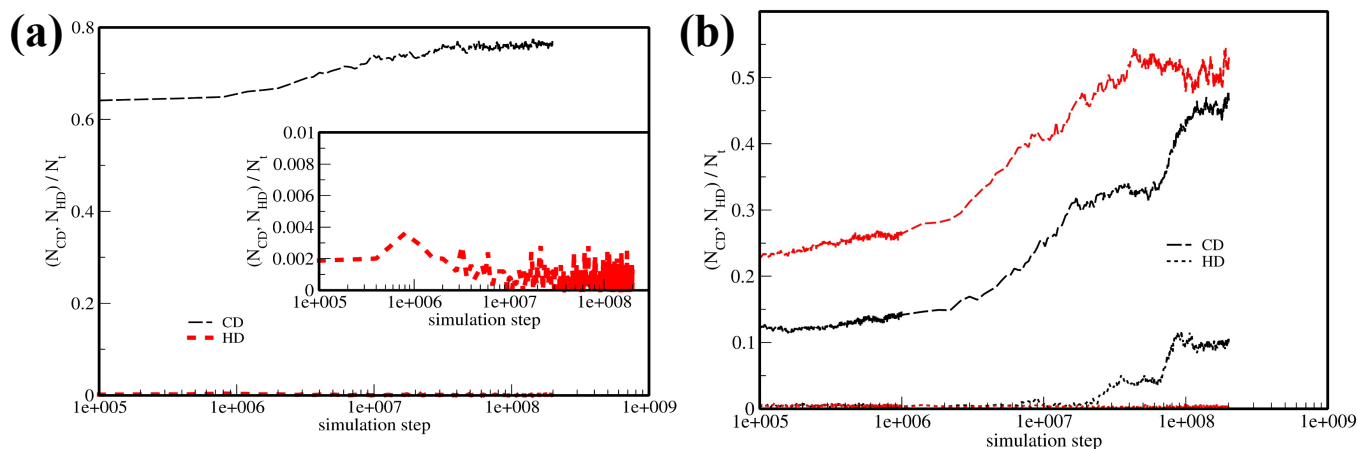


Fig. 6 Parts (a,b): The time evolution of the number of patchy particles belonging to CD and HD networks when the external field is removed for the following conditions, (a) $\xi = 1.0$, $T^* = 0.29$; (b) $\xi = 1.0$ and starting configuration taken from $T^* = 0.33$ (black lines) or $T^* = 0.325$ (red lines) and cooled to $T^* = 0.31$.

ternal field which, if strong enough, causes the adsorption of the first adlayer that is commensurate with the (110) face of a cubic diamond. Such a result is of paramount importance as the cubic polymorph of the diamond-family networks exhibits the complete photonic bandgap making it potentially useful in terms of photonic crystal applications.

In order to comprehensively assess the influence of the applied external field, we evaluated the bulk phase diagram which is of similar type to the one reported for tetrahedral patchy particles modelled with the Kern-Frenkel potential. This suggests that despite using a different approach, our study should not be model-dependent and demonstrate a universal behavior. The latter is strongly supported due to the fact that our findings are based mainly on the geometric commensurability of the two networks. On top of that it was only recently shown that metastable cubic ice can be obtained due to heterogeneous nucleation for an atomistic water model⁴⁵.

Strikingly, once the external field is removed, the formed networks remain stable. This indicates the possibility of further post-synthetic use in which the cubic diamond network could be "washed out" from the surface. Such a procedure is a common practice for the synthesis of 2D materials. Such a finding opens up an avenue for experimental approaches aimed at utilization of tetrahedral patchy particles that not only selectively assemble into a cubic diamond crystal but also can be tested for their photonic applications and specific post-synthetic adjustments can be made.

Eventually, we highlight the importance of using multiple replicas to demonstrate statistically relevant results. On top of that, it is evident that in such systems, the results are subject to strong finite-size effects so the necessity to use sufficiently large systems is crucial.

Conflicts of interest

There are no conflicts to declare.

Acknowledgments

We would like to thank Andrzej Patrykiewicz and Małgorzata Borówko for careful reading of the manuscript and for providing us helpful comments on this article. This work was supported by the National Science Centre, Poland, under Grant No. 2021/41/N/ST4/00437, PRELUDIUM 20.

Notes and references

- 1 P. N. Pusey and W. van Meegen, *Nature*, 1986, **320**, 340–342.
- 2 Z. Cheng, P. Chaikin, W. Russel, W. Meyer, J. Zhu, R. Rogers and R. Ottewill, *Materials & Design*, 2001, **22**, 529–534.
- 3 E. Yablonoitch, *J. Opt. Soc. Am. B*, 1993, **10**, 283–295.
- 4 P. Vukusic, *Physics Today*, 2006, **59**, 82–83.
- 5 M. Maldovan and E. L. Thomas, *Nature Materials*, 2004, **3**, 593–600.
- 6 T. T. Ngo, C. M. Liddell, M. Ghebrebrhan and J. D. Joannopoulos, *Applied Physics Letters*, 2006, **88**, 241920.
- 7 A. B. Rao, J. Shaw, A. Neophytou, D. Morphew, F. Sciortino, R. L. Johnston and D. Chakrabarti, *ACS Nano*, 2020, **14**, 5348–5359.
- 8 F. Romano, E. Sanz and F. Sciortino, *The Journal of Chemical Physics*, 2011, **134**, 174502.
- 9 F. Romano, E. Sanz and F. Sciortino, *The Journal of Chemical Physics*, 2010, **132**, 184501.
- 10 Y.-W. Sun, Z.-W. Li, Z.-Q. Chen, Y.-L. Zhu and Z.-Y. Sun, *Soft Matter*, 2022, **18**, 2654–2662.
- 11 Z.-W. Li, Y.-W. Sun, Y.-H. Wang, Y.-L. Zhu, Z.-Y. Lu and Z.-Y. Sun, *The Journal of Physical Chemistry Letters*, 2021, **12**, 7159–7165.
- 12 F. Romano and F. Sciortino, *Nature Communications*, 2012, **3**, 975.
- 13 D. Morphew, J. Shaw, C. Avins and D. Chakrabarti, *ACS Nano*, 2018, **12**, 2355–2364.
- 14 E. G. Noya, C. Vega, J. P. K. Doye and A. A. Louis, *The Journal of Chemical Physics*, 2010, **132**, 234511.

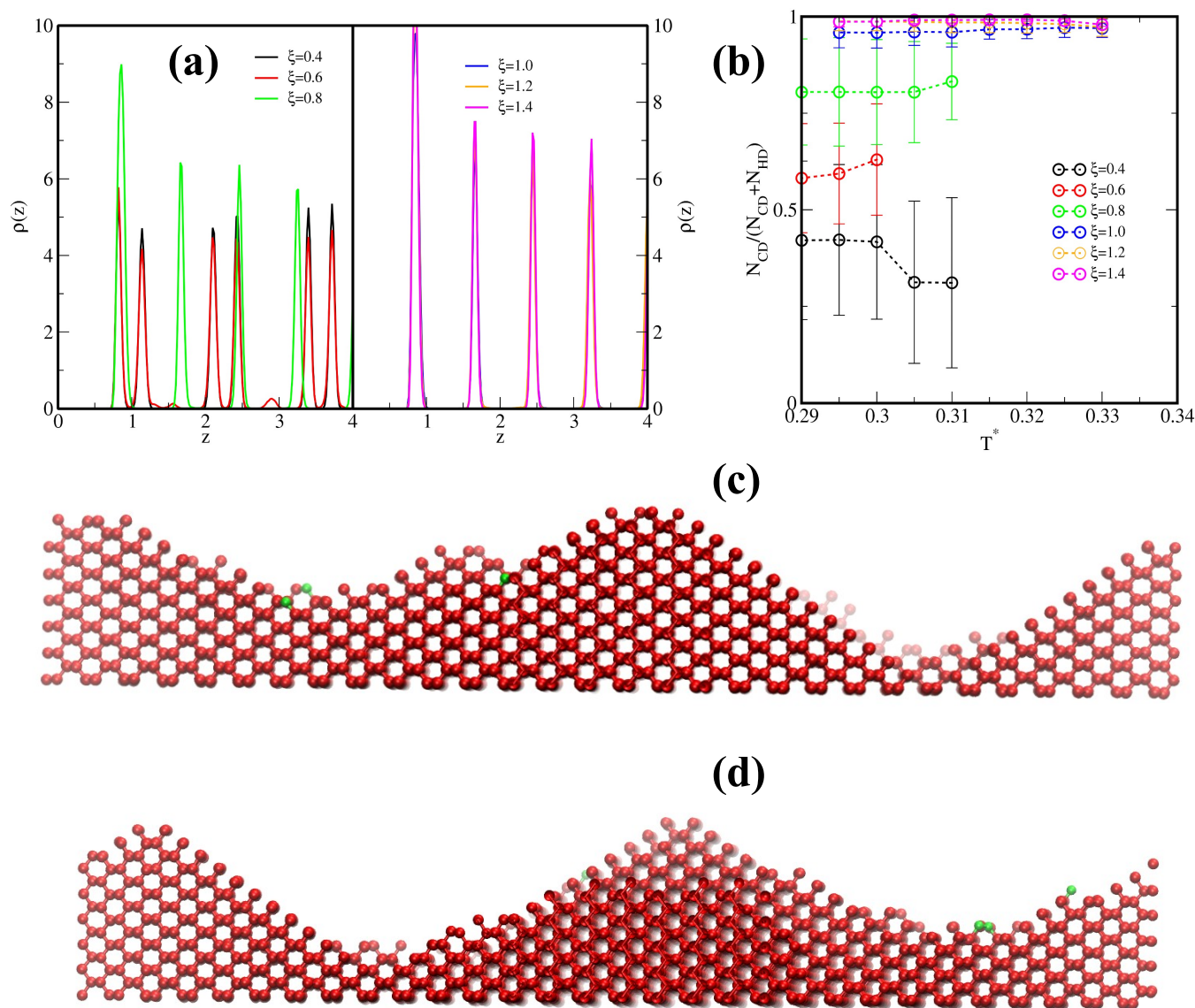


Fig. 7 Part (a): Density profiles for considered systems under different strengths of an applied external field. Part (b): temperature relation of the cubicity parameter for all considered systems. Parts (c), (d): Snapshots for $\xi = 1.0$ and $\xi = 1.2$ at $T^* = 0.3$

- 15 E. G. Noya, I. Zubietta, D. J. Pine and F. Sciortino, *The Journal of Chemical Physics*, 2019, **151**, 094502.
- 16 Zhang, A. S. Keys, T. Chen and S. C. Glotzer, *Langmuir*, 2005, **21**, 11547–11551.
- 17 É. Ducrot, M. He, G.-R. Yi and D. J. Pine, *Nature Materials*, 2017, **16**, 652–657.
- 18 W. Liu, M. Tagawa, H. L. Xin, T. Wang, H. Emamy, H. Li, K. G. Yager, F. W. Starr, A. V. Tkachenko and O. Gang, *Science*, 2016, **351**, 582–586.
- 19 M. He, J. P. Gales, É. Ducrot, Z. Gong, G.-R. Yi, S. Sacanna and D. J. Pine, *Nature*, 2020, **585**, 524–529.
- 20 A. Neophytou, V. N. Manoharan and D. Chakrabarti, *ACS Nano*, 2021, **15**, 2668–2678.
- 21 A. Neophytou, D. Chakrabarti and F. Sciortino, *Proceedings of the National Academy of Sciences*, 2021, **118**, e2109776118.
- 22 L. Rovigatti, J. Russo, F. Romano, M. Matthies, L. Kroc and P. Šulc, *Nanoscale*, 2022, **14**, 14268–14275.
- 23 A. B. Pawar and I. Kretzschmar, *Macromolecular Rapid Communications*, 2010, **31**, 150–168.
- 24 J. Zhang, B. A. Grzybowski and S. Granick, *Langmuir*, 2017, **33**, 6964–6977.
- 25 S. Ravaine and E. Duguet, *Current Opinion in Colloid & Interface Science*, 2017, **30**, 45–53.
- 26 A. Kim, L. Yao, F. Kalutantrige, S. Zhou and Q. Chen, in *Self-Assembly of Nanostructures and Patchy Nanoparticles*, ed. S. Mehraeen, IntechOpen, Rijeka, 2020, ch. 4.
- 27 Y.-J. Kim, J.-B. Moon, H. Hwang, Y. S. Kim and G.-R. Yi, *Advanced Materials*, 2023, **35**, 2203045.
- 28 Ł. Baran and W. Rzyśko, *Mol. Syst. Des. Eng.*, 2020, **5**, 484–492.

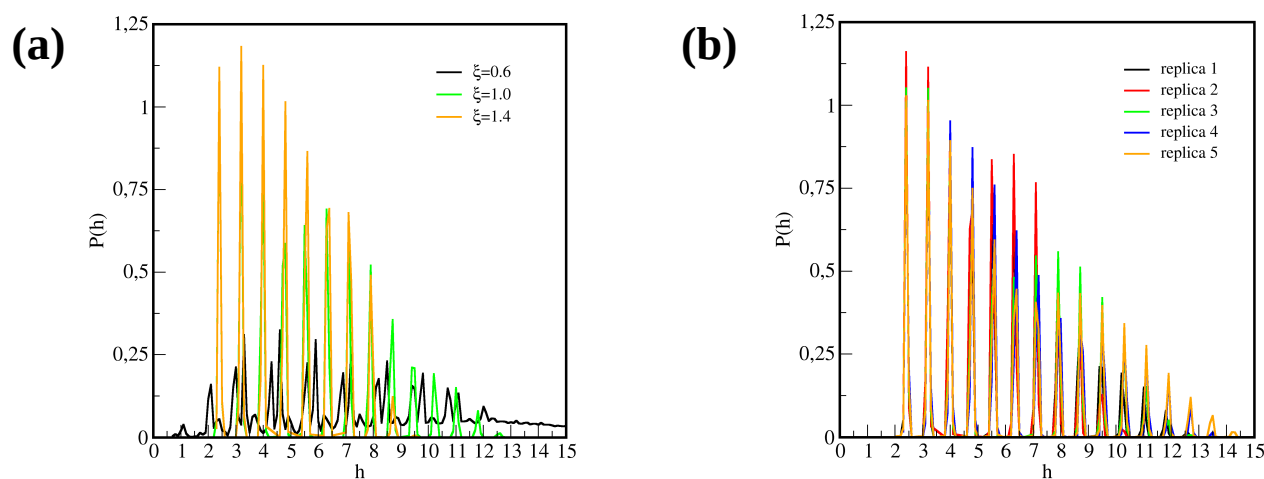


Fig. 8 Part (a): Distribution of the film height for different strength of the surface potential. Part (b): Distribution of the film height for different replicas for the system $\xi = 1.0$ and $T^* = 0.30$.

- 29 Ł. Baran, W. Rżysko and D. Tarasewicz, *Mol. Syst. Des. Eng.*, 2021, **6**, 805–816.
- 30 Y. V. Kalyuzhnyi and P. T. Cummings, *The Journal of Chemical Physics*, 2013, **139**, 104905.
- 31 A. P. Thompson, H. M. Aktulga, R. Berger, D. S. Bolintineanu, W. M. Brown, P. S. Crozier, P. J. in 't Veld, A. Kohlmeyer, S. G. Moore, T. D. Nguyen, R. Shan, M. J. Stevens, J. Tranchida, C. Trott and S. J. Plimpton, *Comp. Phys. Comm.*, 2022, **271**, 108171.
- 32 K. Binder, *Zeitschrift für Physik B Condensed Matter*, 1981, **43**, 119–140.
- 33 P. J. Steinhardt, D. R. Nelson and M. Ronchetti, *Phys. Rev. B*, 1983, **28**, 784–805.
- 34 A. H. Nguyen and V. Molinero, *The Journal of Physical Chemistry B*, 2015, **119**, 9369–9376.
- 35 H. Eslami, K. Bahri and F. Müller-Plathe, *The Journal of Physical Chemistry C*, 2018, **122**, 9235–9244.
- 36 H. Eslami, P. Sedaghat and F. Müller-Plathe, *Phys. Chem. Chem. Phys.*, 2018, **20**, 27059–27068.
- 37 W. Rżysko and A. Trokhymchuk, *The Journal of Chemical Physics*, 2012, **137**, 224505.
- 38 T. L. Malkin, B. J. Murray, C. G. Salzmann, V. Molinero, S. J. Pickering and T. F. Whale, *Phys. Chem. Chem. Phys.*, 2015, **17**, 60–76.
- 39 L. Lupi, A. Hudait, B. Peters, M. Grünwald, R. Gotchy Mullen, A. H. Nguyen and V. Molinero, *Nature*, 2017, **551**, 218–222.
- 40 R. L. Smith, M. Vickers, M. Rosillo-Lopez and C. G. Salzmann, *Crystal Growth & Design*, 2019, **19**, 2131–2138.
- 41 M. Murri, R. L. Smith, K. McColl, M. Hart, M. Alvaro, A. P. Jones, P. Németh, C. G. Salzmann, F. Corà, M. C. Domeneghetti, F. Nestola, N. V. Sobolev, S. A. Vishnevsky, A. M. Logvinova and P. F. McMillan, *Scientific Reports*, 2019, **9**, 10334.
- 42 M. A. Sánchez, T. Kling, T. Ishiyama, M.-J. van Zadel, P. J. Bisson, M. Mezger, M. N. Jochum, J. D. Cyran, W. J. Smit, H. J. Bakker, M. J. Shultz, A. Morita, D. Donadio, Y. Nagata, M. Bonn and E. H. G. Backus, *Proceedings of the National Academy of Sciences*, 2017, **114**, 227–232.
- 43 R. Pandit, M. Schick and M. Wortis, *Phys. Rev. B*, 1982, **26**, 5112–5140.
- 44 A. Patrykiewicz, *International Journal of Molecular Sciences*, 2022, **23**, year.
- 45 M. B. Davies, M. Fitzner and A. Michaelides, *Proceedings of the National Academy of Sciences*, 2021, **118**, e2025245118.

Pursuing Colloidal Diamond

Supporting Information

Łukasz Baran, Dariusz Tarasewicz, Daniel M. Kamiński, Wojciech Rżysko

1 Justification of the chosen model

Model used throughout the current study, was similar as already reported in our previous papers [1, 2]. We found that the choice of the model parameters to be $\sigma_a = 0.2\sigma$, $\varepsilon_{aa} = 5.0\varepsilon$, and $r_{cut} = 2\sigma_a$ is the most efficient to describe relatively strong but reversible associative interactions. The parameter l allows one to the precise control over the desired patch's valency. In order to study diamond phases, we found that $l = 0.36\sigma$ allows for single association of each active sites, resulting in the formation of the total of four bonds per particle. To demonstrate that, Figure S1 displays the distribution of a number of nearest neighbors N_{nn} per particle for three different embedment distances being $l = 0.36\sigma$, $l = 0.40\sigma$, and $l = 0.45\sigma$, calculated up to the first minimum in the radial distribution function $r_{max} = 1.2\sigma$.

One can see that $N_{nn} = 4$ dominates for $l = 0.36\sigma$ and $l = 0.40\sigma$, however, in the case of the latter we see that it can take values between 5 – 7 indicating the possibility that a patch can have higher valency than one. Systems with $l = 0.45\sigma$ take values of $N_{nn} = 9, 12$ as the most probable, indicating the possibility for the formation of fcc/hcp-like crystalline networks which was beyond the scope of current study.

2 Bulk phase diagram

As mentioned in the main text, the phase diagram has been evaluated using block's analysis method proposed by Binder [3]. The distribution functions for several distinct densities and different temperatures are shown in Fig. S2. Part (a) display a regular distribution exhibiting double-peak behavior corresponding to the two-phase coexistence. In present case, we are dealing with the gas-solid coexistence, the latter phase being an hybrid of interwoven hexagonal and cubic diamond polymorphs at around $\rho = 0.71$.

In part (b), on the other hand, one can see that at temperature $T^* = 0.305$ and the density $\rho = 0.4$, there is a gaussian peak, indicating disordered fluid, that is uniformly distributed over an entire system space. This means that in such conditions, we are above the transition temperature into the ordered phase. The same concerns higher densities, however, it needs to be emphasized that suitable transition temperature accordingly increases.

In part (c), we observe large peak around $\rho = 0.71$ corresponding to diamond phases as previously. On the other hand, the low-density peaks vanished which corroborate that gas-solid coexistence is not present under such circumstances. Strikingly, other peaks with slightly lower density than the crystalline phase appear. We conjecture that this is due to the presence of a liquid phase that emerges in a relatively narrow region. Moreover, we did not observe fluctuations between gas and liquid phase within this range of temperatures and for all densities studied, therefore, we envisage this liquid phase is metastable.

In part (d), at higher density, we observe the coexistence between diamond phases and BCC, the latter of which is composed of two interwoven diamond phases. Presence of BCC and other phases has been evaluated by means of the calculation Steinhard order parameter (Eq. 2 and 3 in the main text). The criteria for the discrimination of particular crystalline environments can be found in Table I of the following article [4]. Corresponding snapshots for densities

$\rho = 1.0$ and $\rho = 1.2$ are displayed in Figure S3. In view of all the above, this phase diagram is of a similar type as the ones reported by Romano *et al.* [5, 6], although performed for different interparticle potential.

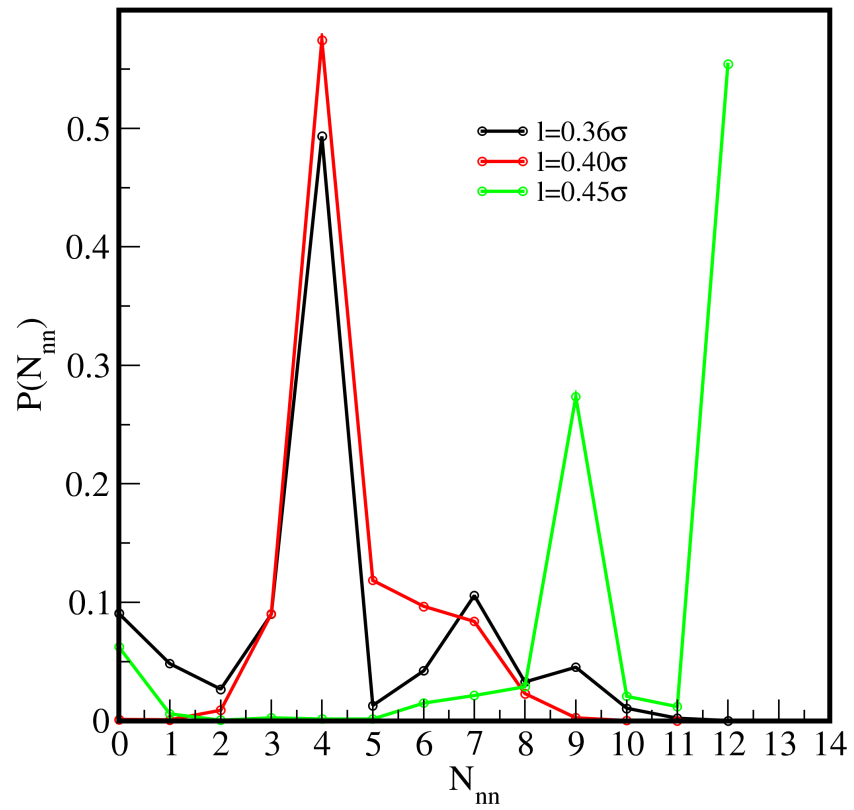


Figure S1: The distribution of the nearest neighbors for systems differing in the embedding distance l .

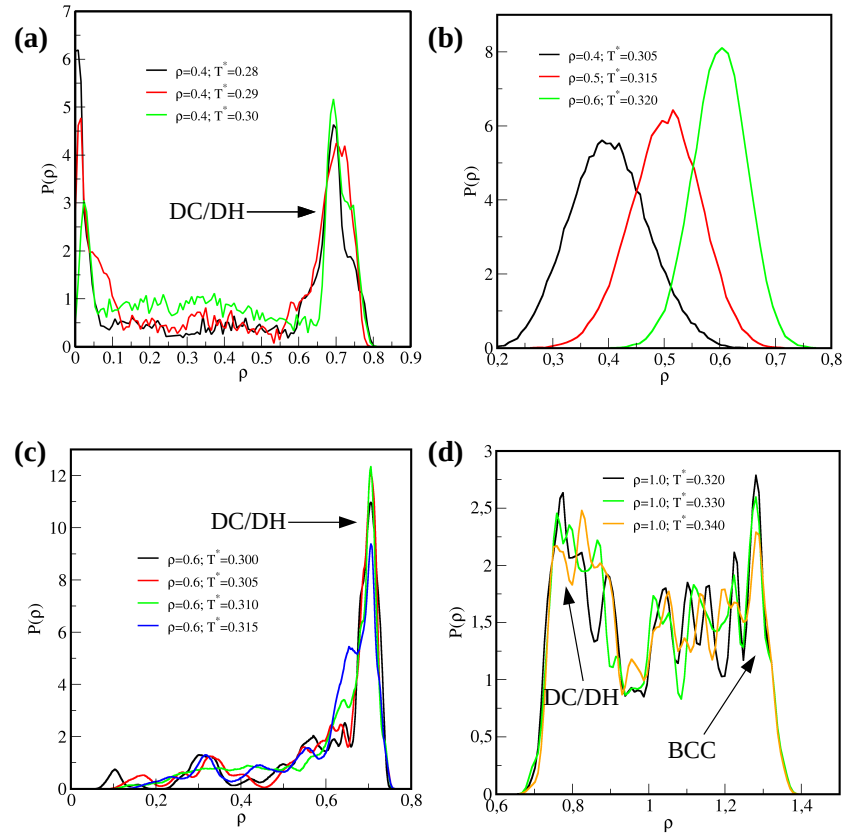


Figure S2: The density distribution functions of the largest block for bulk systems at different densities and temperatures.

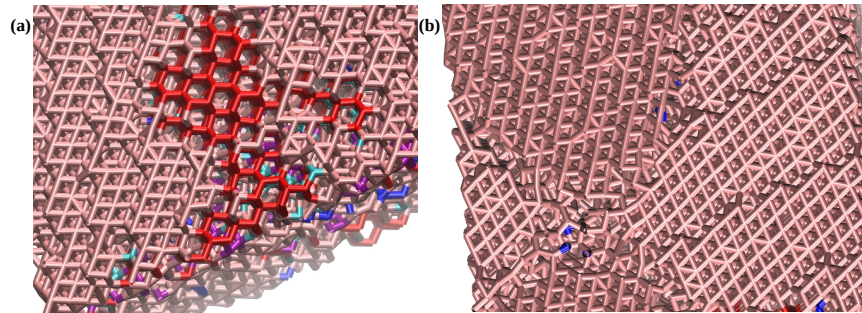


Figure S3: Fragment of the configurations for systems in $\rho = 1.0$ (a) and $\rho = 1.2$ (b) at $T = 0.34$. Red sticks correspond to cubic diamond whereas pink sticks is the remaining fluid.

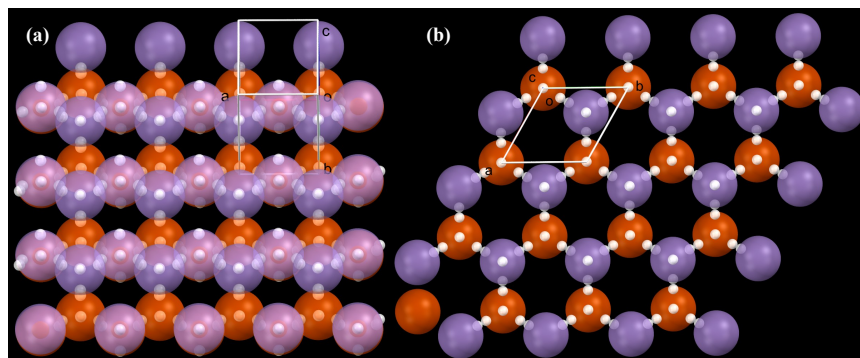


Figure S4: Fragment of the configurations of (a): (110) and (b):(111) faces of cubic diamond formed by tetrahedral patchy particles for systems $\xi = 1.0$ (a) and $\xi = 0.4$ (b). Yellow and purple atoms correspond to the lower and upper layer, respectively. White spheres schematically represent the active sites.

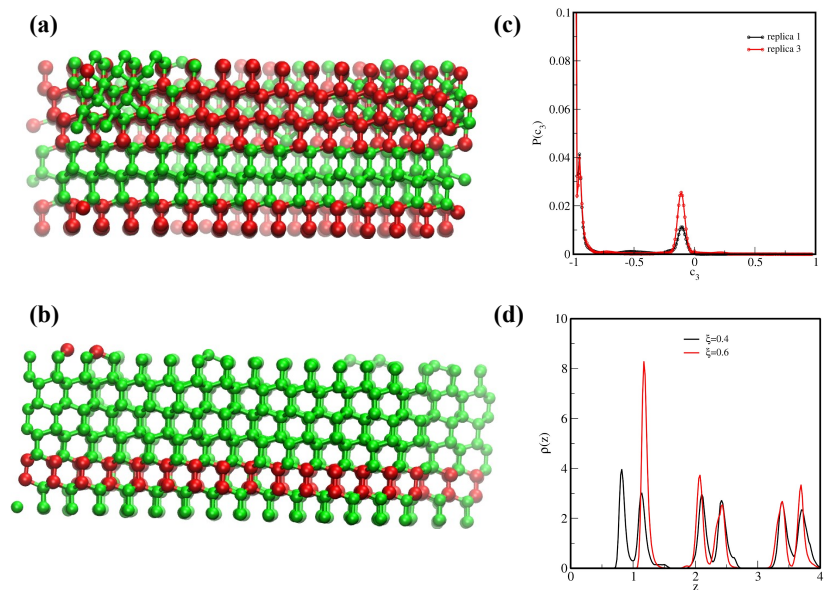


Figure S5: Parts (a, b): Snapshots of two different replicas, differing in the ratio of two cubic polymorphs in the stacking hybrids. Part (c): Distribution function of the order parameter $P(c_3)$ for replicas shown in parts (a, b). Part (d): Comparison of density profiles for $\xi = 0.4$ and $\xi = 0.6$. The latter is shifted by $1/3\sigma$ in the z-direction (cf. Main text).

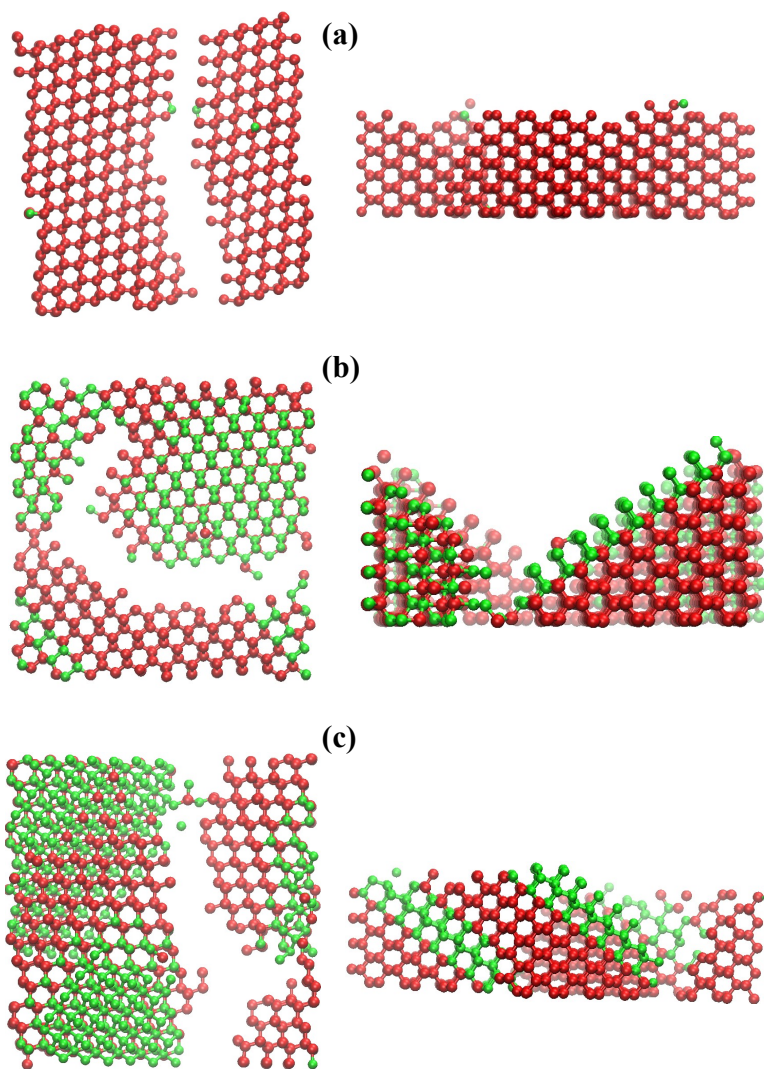


Figure S6: Snapshots for three different replicas for system $\xi = 1.0$ at $T^* = 0.30$. Left and right panels correspond to top and front view, respectively.

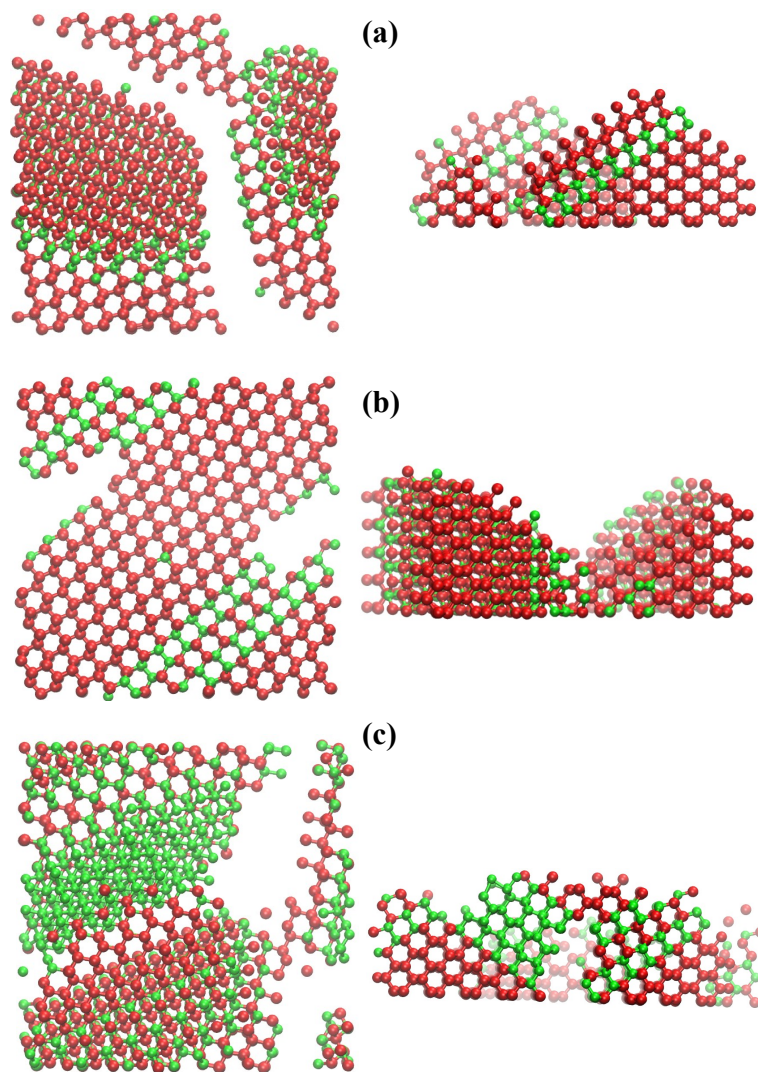


Figure S7: Snapshots for three different replicas for system $\xi = 1.2$ at $T^* = 0.30$. Left and right panels correspond to top and front view, respectively.

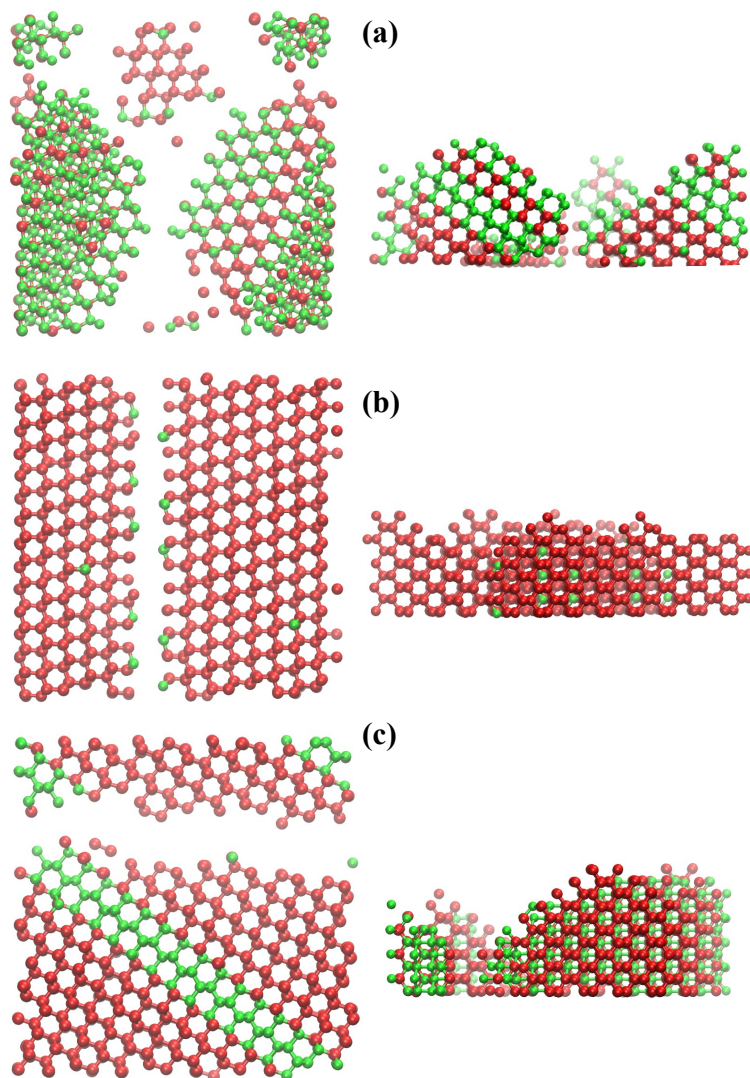


Figure S8: Snapshots for three different replicas for system $\xi = 1.4$ at $T^* = 0.30$. Left and right panels correspond to top and front view, respectively.

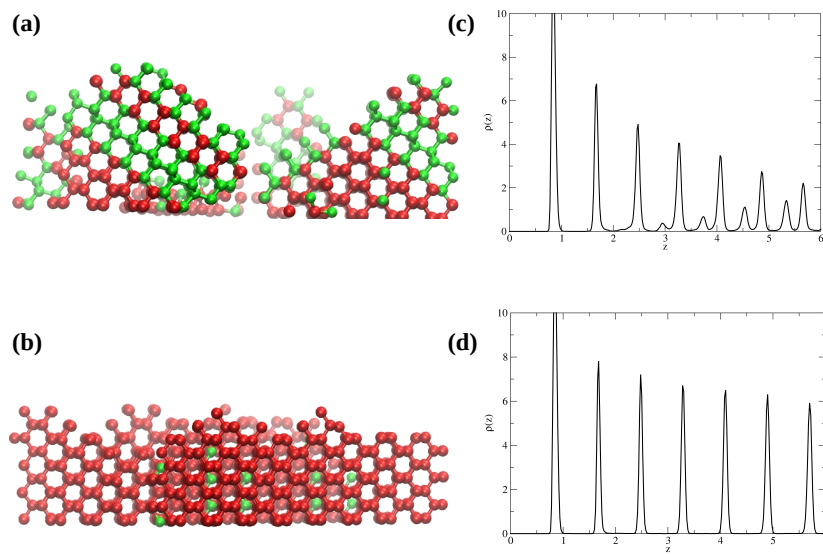


Figure S9: Parts (a, b): Snapshots for two different replicas for system $\xi = 1.4$ at $T^* = 0.30$. Parts (c, d): Density profiles for replicas shown in parts (a, b) with tilted (c) and flat growth of the crystal (d).

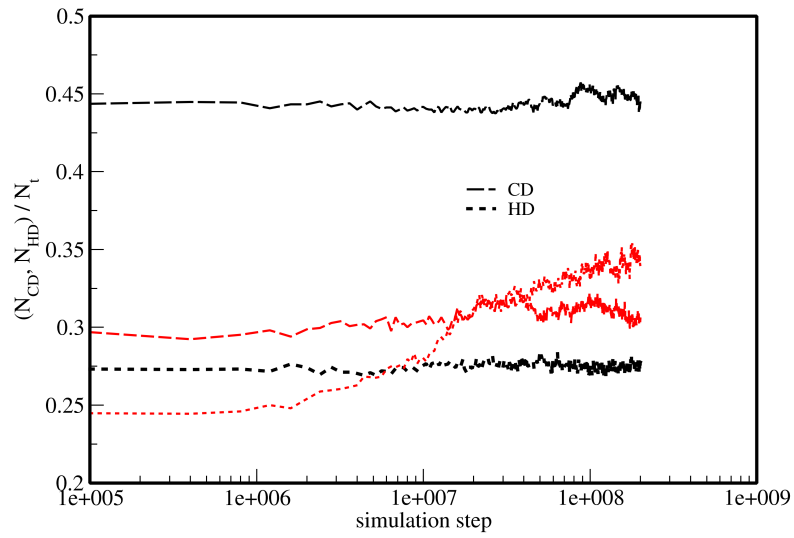


Figure S10: The time evolution of the number of patchy particles belonging to CD and HD networks when the external field is removed for $\xi = 0.4$, $T^* = 0.29$ (black lines) and $\xi = 0.6$, $T^* = 0.29$ (red lines)

References

- [1] Ł. Baran and W. Rżysko, “Application of a coarse-grained model for the design of complex supramolecular networks,” *Mol. Syst. Des. Eng.*, vol. 5, pp. 484–492, 2020.
- [2] Ł. Baran, W. Rżysko, and D. Tarasewicz, “Variation of interaction zone size for the target design of 2d supramolecular networks,” *Mol. Syst. Des. Eng.*, vol. 6, pp. 805–816, 2021.
- [3] K. Binder, “Finite size scaling analysis of ising model block distribution functions,” *Zeitschrift für Physik B Condensed Matter*, vol. 43, pp. 119–140, 1981.
- [4] W. Mickel, S. C. Kapfer, G. E. Schröder-Turk, and K. Mecke, “Shortcomings of the bond orientational order parameters for the analysis of disordered particulate matter,” *The Journal of Chemical Physics*, vol. 138, no. 4, p. 044501, 2013.
- [5] F. Romano, E. Sanz, and F. Sciortino, “Crystallization of tetrahedral patchy particles in silico,” *The Journal of Chemical Physics*, vol. 134, no. 17, p. 174502, 2011.
- [6] F. Romano, E. Sanz, and F. Sciortino, “Phase diagram of a tetrahedral patchy particle model for different interaction ranges,” *The Journal of Chemical Physics*, vol. 132, no. 18, p. 184501, 2010.